Journal of Experimental Botany, Vol. 64, No. 11, pp. 3249–3260, 2013
doi:10.1093/jxb/ert160
This paper is available online free of all access charges (see http://jxb.oxfordjournals.org/open_access.html for further details)

Journal of Experimental Botany
www.jxb.oxfordjournals.org

RESEARCH PAPER

Pattern of iron distribution in maternal and filial tissues in wheat grains with contrasting levels of iron

Sudhir P. Singh[1], Katarina Vogel-Mikuš[2], Iztok Arčon[3,4], Primož Vavpetič[4], Luka Jeromel[4], Primož Pelicon[4], Jitendra Kumar[1] and Rakesh Tuli[1,*]

[1] National Agri-Food Biotechnology Institute, Department of Biotechnology, C-127, Industrial Area, Phase-8, Mohali 160071, India
[2] Department of Biology, Biotechnical Faculty, University of Ljubljana, Večna pot 111, SI-1000 Ljubljana, Slovenia
[3] University of Nova Gorica, Vipavska 13, POB 301, SI-5001 Nova Gorica, Slovenia
[4] Jožef Stefan Institute, Jamova 39, SI-1000 Ljubljana, Slovenia

* To whom correspondence should be addressed. E-mail: rakeshtuli@hotmail.com

Received 11 March 2013; Revised 4 May 2013; Accepted 8 May 2013

Abstract

Iron insufficiency is a worldwide problem in human diets. In cereals like wheat, the bran layer of the grains is an important source of iron. However, the dietary availability of iron in wheat flour is limited due to the loss of the iron-rich bran during milling and processing and the presence of anti-nutrients like phytic acid that keep iron strongly chelated in the grain. The present study investigated the localization of iron and phosphorus in grain tissues of wheat genotypes with contrasting grain iron content using synchrotron-based micro-X-ray fluorescence (micro-XRF) and micro-proton-induced X-ray emission (micro-PIXE). X-ray absorption near-edge spectroscopy (XANES) was employed to determine the proportion of divalent and trivalent forms of Fe in the grains. It revealed the abundance of oxygen, phosphorus, and sulphur in the local chemical environment of Fe in grains, as Fe-O-P-R and Fe-O-S-R coordination. Contrasting differences were noticed in tissue-specific relative localization of Fe, P, and S among the different genotypes, suggesting a possible effect of localization pattern on iron bioavailability. The current study reports the shift in iron distribution from maternal to filial tissues of grains during the evolution of wheat from its wild relatives to the present-day cultivated varieties, and thus suggests the value of detailed physical localization studies in varietal improvement programmes for food crops.

Key words: Biofortification, grain iron distribution, micro-PIXE, *Triticum aestivum*, XANES, micro-XRF.

Introduction

Iron deficiency is the most prevalent micronutrient insufficiency, affecting more than 1.6 billion people worldwide, particularly women and children (Grimm *et al.*, 2012). The diet in resource-poor countries is based on staple cereal grains which are particularly poor sources of iron (Lee *et al.*, 2012). Cultivation for high yields has led breeders to develop varieties for high yields rather than nutritional quality, leading to an inadvertent rise in mineral deficiency (Zhao *et al.*, 2009). In order to enhance the level of iron in grains and their dietary availability, it is important to understand the uptake, transport, and distribution of iron in plants and sink organs and their relationship with plant growth and development and dietary bioavailability.

Graminaceous plants have evolved a distinct mechanism for iron uptake, known as 'chelation' strategy, which is similar to that of many bacteria and fungi. This strategy is considered as an adaptation to alkaline soils where acidification of the rhizosphere is difficult (Ma and Nomoto, 1996). Root cells secrete phytosiderophores to strongly chelate iron and take up the Fe(III)–phytosiderophore complex via transporters called Yellow Stripe1 (YS1) (Curie *et al.*, 2001). Inside the root cells, iron is complexed with nicotianamine acid and moves

symplastically through the interconnected cytoplasm. Iron is then effluxed into the vascular system for long-distance transport and is unloaded into the sink tissues: buds, tips, and seeds (Hell and Stephan, 2003; Morrissey and Guerinot, 2009). During grain development, metal ions are remobilized from leaves to developing grains via phloem tissues, due to xylem discontinuity and seeds being non-transpiring organs (Hell and Stephan, 2003; Tanaka *et al.*, 2007). In the wheat grains, vascular cells are embedded in the ground tissue (parenchyma which retains protoplasm in the cells), which serves as a symplastic compartment for delivering the imported nutrients into the specialized apoplasmic endosperm cavity. Nutrients are retrieved from the endosperm cavity by specialized transfer cells of the aleurone located at the interface of maternal and filial tissue (Patrick and Offler, 2001).

When developing biofortification strategies for a grain, it is important to understand the localization of iron in different tissues within the seed (Conte and Walker, 2011). Very little is known about mineral distribution in different tissues and specific cell types in grains (Stomph *et al.*, 2011). In wheat grains, iron is located in the outer bran layers, most of which is lost during milling and processing (Zhang *et al.*, 2010; Regvar *et al.*, 2011). The flour is almost devoid of iron. Hence, the development of wheat varieties with iron-enriched endosperm offers an important strategy to enhance dietary availability of iron in wheat flour. It is important to understand both the pathways that lead to the accumulation of iron in the aleurone layer and the bottlenecks that prevent its translocation from the outer bran layers into the endosperm. This study aims at exploring if there are differences in the mineral transport across different tissues and between wheat genotypes with contrasting levels of grain iron. Only a few studies have been made on the distribution of minerals in wheat grains (Regvar *et al.*, 2011; Stomph *et al.*, 2011) and barley (Lombi *et al.*, 2011).

The spatial distribution of metals within biological tissues can be studied using micro-analytical techniques based on the emission of characteristic X-rays, excited either by charged particles (electrons, protons, or heavier particles) or photons (synchrotron radiation) (Vogel-Mikuš *et al.*, 2008; Moore *et al.*, 2010; Regvar *et al.*, 2011). Synchrotron-based micro-X-ray fluorescence (micro-XRF) allows the mapping of element distributions at the tissue, cellular, and subcellular levels and the *in situ* detection of chemical forms of elements by X-ray absorption near-edge structure spectroscopy (XANES). The only drawback of element distribution imaging employing micro-XRF is the absence of suitable software for fully quantitative analysis. Studies using micro-XRF can provide elemental distribution maps constructed by displaying the number of counts integrated over the energy window, corresponding to the strongest Kα or Lα lines of the mapped elements or integrated after X-ray spectra deconvolution, using software such as PyMCA (Solé *et al.*, 2007) and normalization to dwell time and beam current (Lombi *et al.*, 2011; Regvar *et al.*, 2011; Tolrà *et al.*, 2011; Hansen *et al.*, 2012). This makes the element distribution maps of tissues and cells of different origin and/or treatment and those recorded under different experimental conditions difficult to compare. Micro-proton-induced X-ray emission (micro-PIXE) on the other hand, offers fully quantitative element distribution analysis. In combination with scanning transmission ion microscopy (STIM), which provides the lateral thickness distribution of the sample, micro-PIXE enables elemental mapping and quantification of elemental concentrations in tissue sections (Mesjasz-Przybyłowicz and Przybyłowicz, 2002; Vogel-Mikuš *et al.*, 2008).

The present study was aimed at investigating the distribution and chemical forms of iron in seed tissues of wheat genotypes with contrasting grain iron content. The micro-X-ray fluorescence-based imaging techniques do not require chemical destruction or milling of the grain to reveal the elemental composition of tissues or cell layers. micro-XRF and micro-PIXE were utilized to reveal iron localization and tissue-specific concentrations in seeds of four genotypes with differences in grain iron content. Fe K-edge XANES was employed to study the relative amounts of different valence states of iron present in the whole grain and to identify the dominant chemical environments around iron atoms in the grain tissues.

Materials and methods

Plant material

Diverse genotypes of wheat were sown on the experimental field of National Agri-Food Biotechnology Institute (NABI), SAS Nagar (Mohali) Punjab, India (310 m above sea level; 30° 47′ N 76° 41′ E) during the last week of October 2010. Mature grains were collected during April 2011 from genotypes with different grain iron concentration. *Triticum aestivum* L. IITR26 and its wild relative, *Aegilops kotschyi* acc. 3790, have 2- and 3-times more grain iron, respectively, than the cultivars *T. aestivum* Cv. WH291 and *T. aestivum* Cv. WL711 (Supplementary Fig. S1A, available at *JXB* online).

Sample preparation for micro-XRF and micro-PIXE analysis

The seeds were harvested along with the husk. The husk was removed with plastic forceps to extract the seeds, which were wiped with moist paper towel before the analysis. For micro-XRF analysis, the mature dried grains were cut transversely into 2-mm-thick sections with a stainless steel scalpel, which were then individually mounted on a piece of Kapton polyimide film for micro-XRF studies. For micro-PIXE analysis, the mature dried grains were imbibed for 2 hours, dipped in tissue-freezing medium (Jung, Leica), and rapidly frozen in liquid propane cooled by liquid nitrogen (Vogel-Mikuš *et al.*, 2008). The grains were then transferred to a cryomicrotome (CM3050, CM1950 Leica Microsystems, Germany) and sectioned to 30-µm-thick cross-sections (Vogel-Mikuš *et al.*, 2009). The temperature of the microtome head and the chamber was in the range from –25 to –20 °C. The cross-sections were placed in pre-cooled aluminium holders, transferred to an Alpha 2–4 Christ freeze dryer using a cryo-transfer-assembly cooled by liquid nitrogen, and freeze dried at –30°C at a pressure of 0.3 mbar for 3 days. Dry grain cross-sections were mounted on the aluminium sample holder between two thin layers of Pioloform foil.

Micro-XRF analysis

A hard X-ray microprobe beamline, VESPERS (very sensitive elemental and structural probe employing radiation from a synchrotron), was used for micro-XRF studies on grain sections at Canadian Light Source (CLS), Saskatoon, Canada. The beamline is equipped

with compound optics and a double crystal/multilayer monochromator and is capable of delivering both polychromatic (5–30 keV) and monochromatic beams with bandwidth of 0.01, 1.6, and 10%. A pair of KB mirrors is used to focus the beam down to a spot size of 2 × 2 μm. Polychromatic beam was used for micro-XRF work to generate fluorescence spectrum from the sample. A step-by-step micro-XRF scan was performed in the air in both horizontal and vertical directions with 10 μm step-size. Dwell time on each pixel is 1 second. The fluorescence spectra on each pixel were recorded by a four-element Vortex silicon drift detector placed perpendicular to the beam path at a distance of 40 mm. Element maps were generated from these fluorescence spectra using either beamline software (online) or PyMCA (offline) (Solé *et al.*, 2007).

Micro-PIXE analysis

Micro-PIXE measurements and data analysis of grain sections were performed using nuclear microprobe at Jožef Stefan Institute as described previously (Vogel-Mikuš *et al.*, 2008, 2009; Lyubenova *et al.*, 2012). A proton beam with the energy of 2.5 MeV, 400 pA, and the size of $1.5 \times 1.7\ \mu m^2$ was raster scanned across the square-shaped area of selected size. The detection events at five simultaneously operated detectors (low-energy X-ray detector, high-energy X-ray detector, on-off axis STIM detector, elastic backscattering spectrometry (EBS) detector, and chopper EBS detector) were recorded in a list mode together with the corresponding beam position. Distinct morphological structures such as the testa, aleurone, endosperm, scutellum, and embryo were identified using STIM and the corresponding element distribution maps. Assuming a cellulose matrix, the average thickness of the selected area was calculated from the STIM spectrum and used for matrix corrections in the GEOPIXE II software package (CSIRO Earth Science and Resource, Clayton, Australia) (Ryan, 2000), which was used also for fitting of obtained PIXE spectra and generation of quantitative element-distribution maps. The calibration of the PIXE method was verified by the analysis of the multi-elemental standard reference materials NIST SRM 1573a (tomato leaves, homogenized powder, analysed in a form of pressed pellet), NIST SRM 1107 (naval brass B, alloy), and NIST SRM 620 (soda-lime flat glass). The inter-calibration of PIXE and STIM was verified by thin mono-elemental metallic foils.

XANES analysis

Intact grains (n = 10–15) were fixed on aluminium holders using scotch tape (free of Fe). X-ray absorption spectra were measured on intact grains in the fluorescence mode at C beamline of Hamburger Synchrotronstrahlungslabor (HASYLAB) synchrotron, DESY, Hamburg, Germany. The station provided unfocused beam. A pair of horizontal and vertical slits allowed the reduction of the beam size on the sample to about 5 × 1 mm, illuminating major part of the grains in the holder. A silicon (Si 111) double crystal monochromator was used with 1 eV resolution at the Fe K-edge (7112 eV). Harmonics were effectively eliminated by detuning the second monochromator crystal, keeping the intensity at 60% of the rocking curve with the beam stabilization feedback control. The intensity of the monochromatic X-ray beam was measured by three consecutive 10-cm-long ionization chambers, first filled with 950 mbar nitrogen, second and third with argon at pressures of 390 and 500 mbar, respectively.

The samples were inserted between the first and the second ionization cells and positioned at the angle of 45° relative to the beam direction. A seven-pixel SDD fluorescence detector, positioned at 90° relative to the beam direction, was used to measure the intensity of the Fe-K_α fluorescence radiation. The fluorescence spectra were obtained as the ratio of the fluorescence detector signal and the signal of the incident photon beam from the first ionization chamber with the integration time of 4 or 1 s/step. Two repetitions were taken to check the reproducibility of individual scans and to improve the signal-to-noise ratio. No evidence of Fe K-edge shifts in consecutive scans of the samples was observed due to the absorbed dose of ionizing radiation.

Exact energy calibration was established with simultaneous absorption measurements on a 5-μm-thick Fe metal foil placed between the second and the third ionization chamber in all experiments. Zero energy was taken at the first inflection point in the Fe metal spectrum (7112 eV), i.e. at the 1s ionization threshold in the Fe metal. Absolute energy reproducibility of the measured spectra was ± 0.03 eV or better.

The reference complexes of Fe and organic ligands (Fe(II) glutathione and Fe(II) phytate, Fe(II) sulphate, Fe(II) oxalate, Fe(III) phytate, Fe(III) sulphate, Fe(III) citrate) were prepared from $FeCl_2.4H_2O$ or $FeCl_3.6H_2O$ by mixing Fe compound and organic ligand in 1:10 molar ratio. $Fe_2O_{12}S_{3x}H_2O$, $FePO_4$, $Fe_2(C_4H_4O_6)_3$, $C_2FeO_4.2H_2O$, $C_6H_5FeO_7.H_2O$, Fe_3O_4, α-FeOOH, and Fe_2O_3 were thoroughly mixed with pure microcrystalline cellulose and pressed into pellets with total absorption thickness of about 2.

The analysis of XANES spectra was performed with the IFEFFIT program package ATHENA (Ravel and Newville, 2005). The relative K-shell contribution in the absorption spectra measured in transmission detection mode was obtained by removing the extrapolated best-fit linear function determined in the pre-edge region (–50 to –20 eV). By conventional normalization, extrapolating the post-edge spline background, determined in the range from 12 to 90 eV, the Fe K-edge jump was set to 1.

Results

Micro-XRF maps

Micro-XRF imaging was conducted by focussing the beam on the crease region to analyse the spatial distribution of iron in mature seeds of genotypes with contrasting grain iron content. The crease is a mass of tissue placed in the ventral groove formed by the fusion of two maternal tissues, the funiculus (the stalk that joins the ovule to the carpel wall) and the chalaza. In wheat seeds, nutrients are unloaded from the vascular tissue/strand that runs along the crease (Pearson *et al.*, 1995). Nutrients supplied by the mother plant to the developing grain are transported through the maternal tissues of the crease to the endosperm (Stomph *et al.*, 2011). The mineral transport route within the grain comprises of the pigment or vascular strand, the nucellar projection, the endosperm cavity, the aleurone transfer cells (bordering the endosperm cavity), and the subsequent layers of endosperm (Supplementary Fig. S1B).

In all four genotypes, the aleurone layer was a hot spot for the accumulation of iron, with significantly very low signals in the endosperm (Fig. 1). The high-iron genotypes (*A. kotschyi* acc. 3790 and *T. aestivum* L. IITR26) showed a relatively high intensity of iron in the region of the pigment strand and the nucellar projection of the crease (Fig. 1A,B). In the low-iron cultivars (*T. aestivum* Cv. WH291 and *T. aestivum* Cv.WL711), the high-intensity region was towards the aleurone of the crease (Fig. 1C,D).

Qualitative and quantitative mapping of iron distribution

Micro-PIXE spectroscopy is an efficient technique for qualitative and quantitative elemental distribution mapping in biological samples, without chemical destruction (Vogel-Mikuš *et al.*, 2009; Pongrac *et al.*, 2011). Micro-PIXE was applied on cross-sections of whole grains and crease regions of the four genotypes. The micro-PIXE elemental imaging validated the localization of iron revealed by micro-XRF and also determined the iron concentrations within the tissues (Fig. 2).

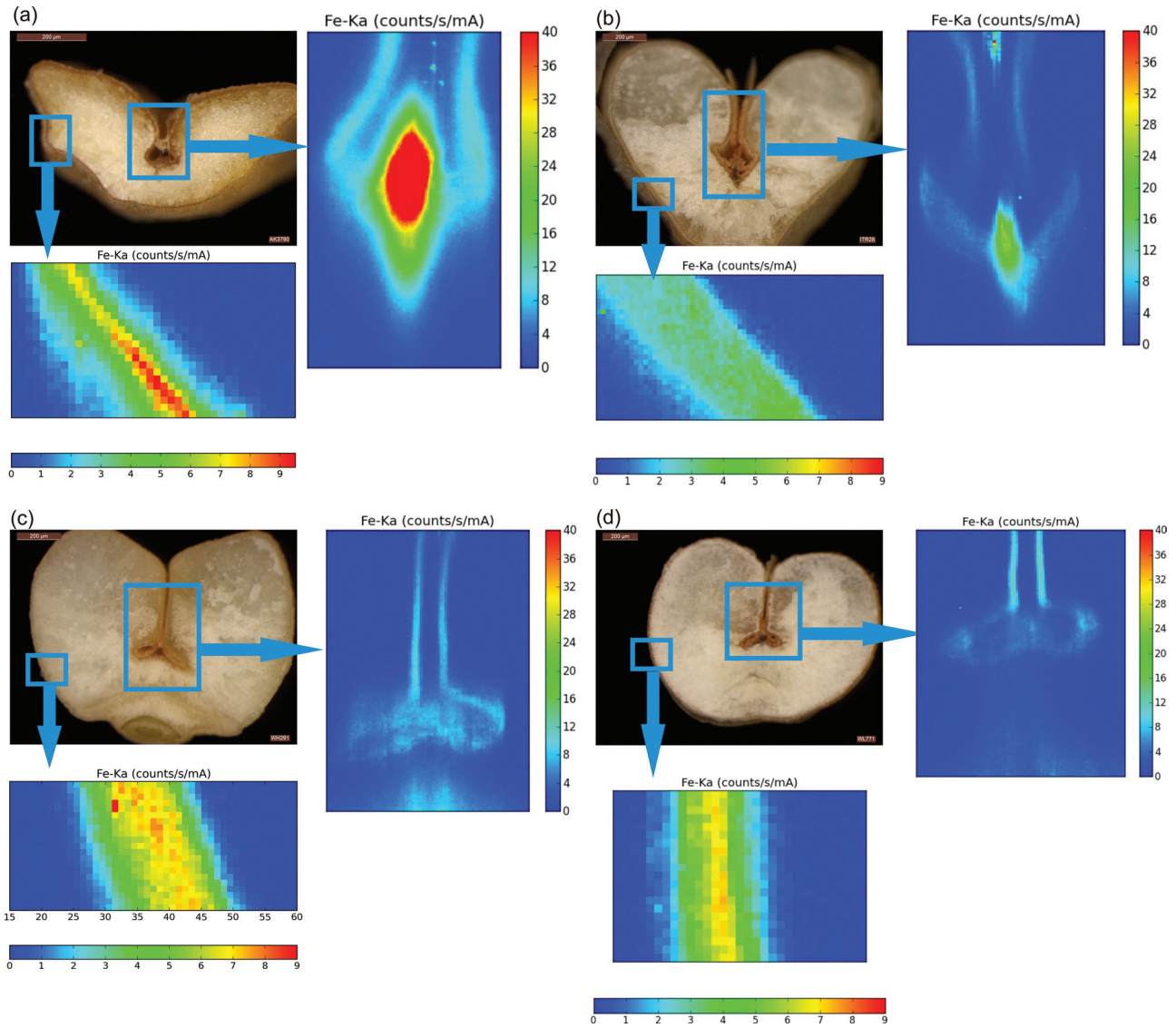

Fig. 1. Micro-XRF maps of cross-sectioned seeds of *A. kotschyi* acc. 3790 (A), *T. aestivum* L. IITR26 (B), *T. aestivum* Cv. WH291 (C), and *T. aestivum* Cv. WL711 (D). The insets mark the regions of crease and aleurone for which magnified XRF maps are shown. The colour scale represents relative intensity of fluorescence, with blue and red corresponding to the lowest and highest accumulation of iron, respectively. Intensities of iron K-α line are expressed in counts s^{-1} mA^{-1}.

In the case of *A. kotschyi* acc. 3790, a higher concentration of iron was observed in the crease region, particularly in the vascular strand. The other iron-rich tissues were the nucellar projection, the crease aleurone, the aleurone, and the scutellum (Fig. 2A,E,F). The endosperm showed very low iron accumulation.

Analysis of the iron distribution in *T. aestivum* L. IITR26 established the nucellar projection as carrying the highest concentration. The next iron-rich tissues were the crease aleurone, the aleurone, and the scutellum. In the pigment strand, iron concentration was more than 6-times lower than in the nucellar projection, indicating the mobilization of iron from the vascular tissue to the nucellar projection (Fig. 2B,E,F).

Micro-PIXE element maps of the low-iron cultivars depicted the crease aleurone, the nucellar projection, and the aleurone as major tissues for iron accumulation and localization, followed by the scutellum and the vascular strand (Fig. 2C–F). In the nucellar projection, iron concentration was significantly less than in the aleurone.

Along the mineral transport route (from vascular tissue to the nucellar projection to the crease-aleurone), in contrast to the high-iron genotypes, a gradual increase in iron concentration was observed in both low-iron genotypes (Fig. 3C,D). In the case of the land race, a higher peak was apparent in the nucellar projection of the crease region, unlike in the two low-iron cultivars (Fig. 3B). On the other hand, in *A. kotschyi*, iron predominantly accumulated in the pigment strand (Figs. 2F and 3A).

The iron accumulation pattern in the whole grain affirms the aleurone and the scutellum as iron-rich grain tissues in all genotypes (Fig. 2E). The most noticeable feature in all

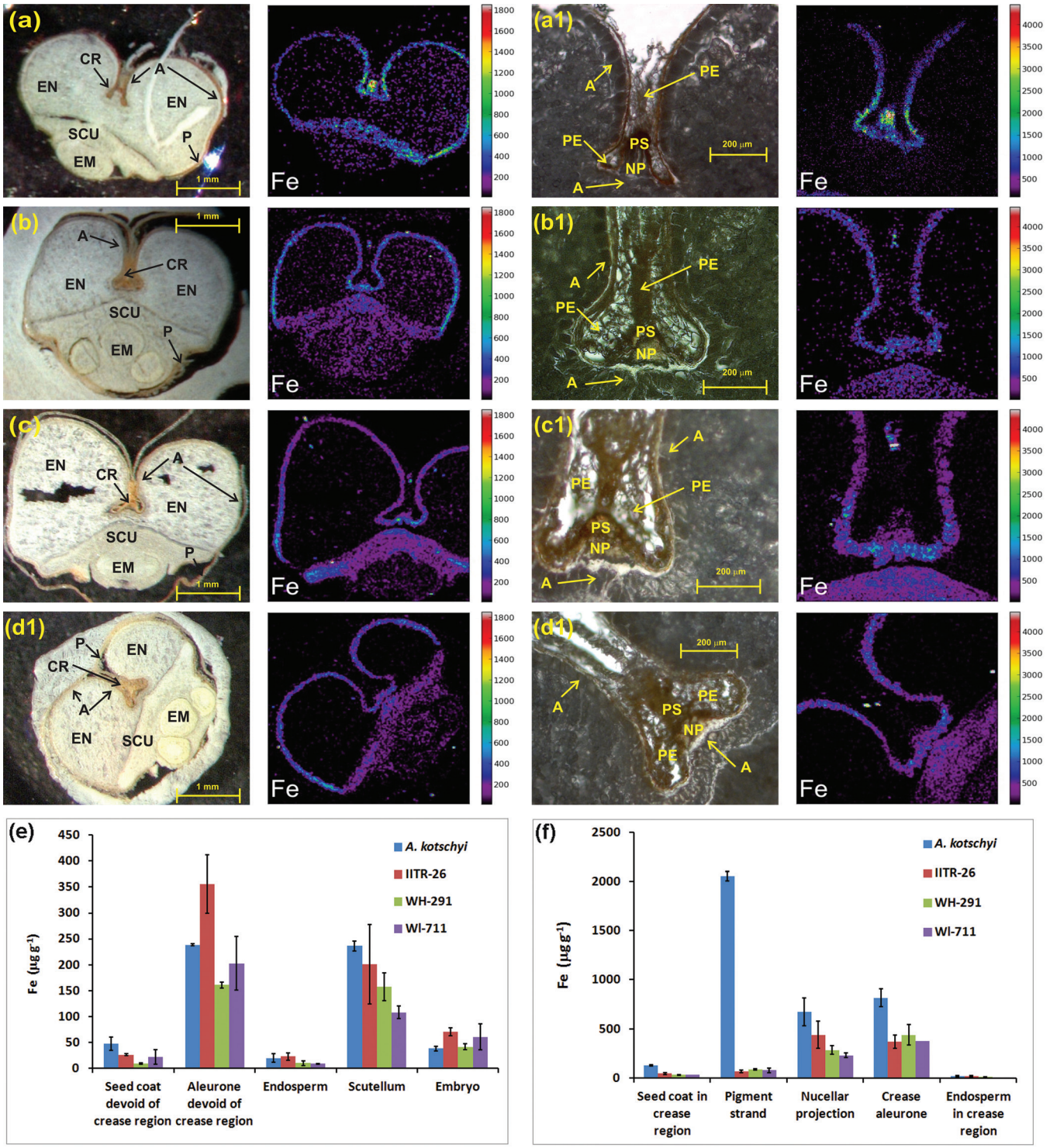

Fig. 2. (A–D) Micro-PIXE images showing iron localization in cross-section of whole grain (left) and crease tissues (right) of *A. kotschyi* acc. 3790 (A), *T. aestivum* L. IITR26 (B), *T. aestivum* Cv. WH291 (C), and *T. aestivum* Cv. WL711 (D). (E, F) Iron accumulation patterns based on iron concentration in grain (E) and crease tissues (F) of the four genotypes. Values are mean ± SE µg (g dryweight)$^{-1}$ from selected tissues (Fig. S2) of two independently measured cuttings. The aleurone and seed coat in E are devoid of crease region. The endosperm in F corresponds only to the region around the crease. A, aleurone; CR, crease; EM, embryo; EN, endosperm; NP, nucellar projection; P, peripheral tissues (pericarp and seed coat); PE, pericarp; PS, pigment (vascular) strand; SCU, scutellum.

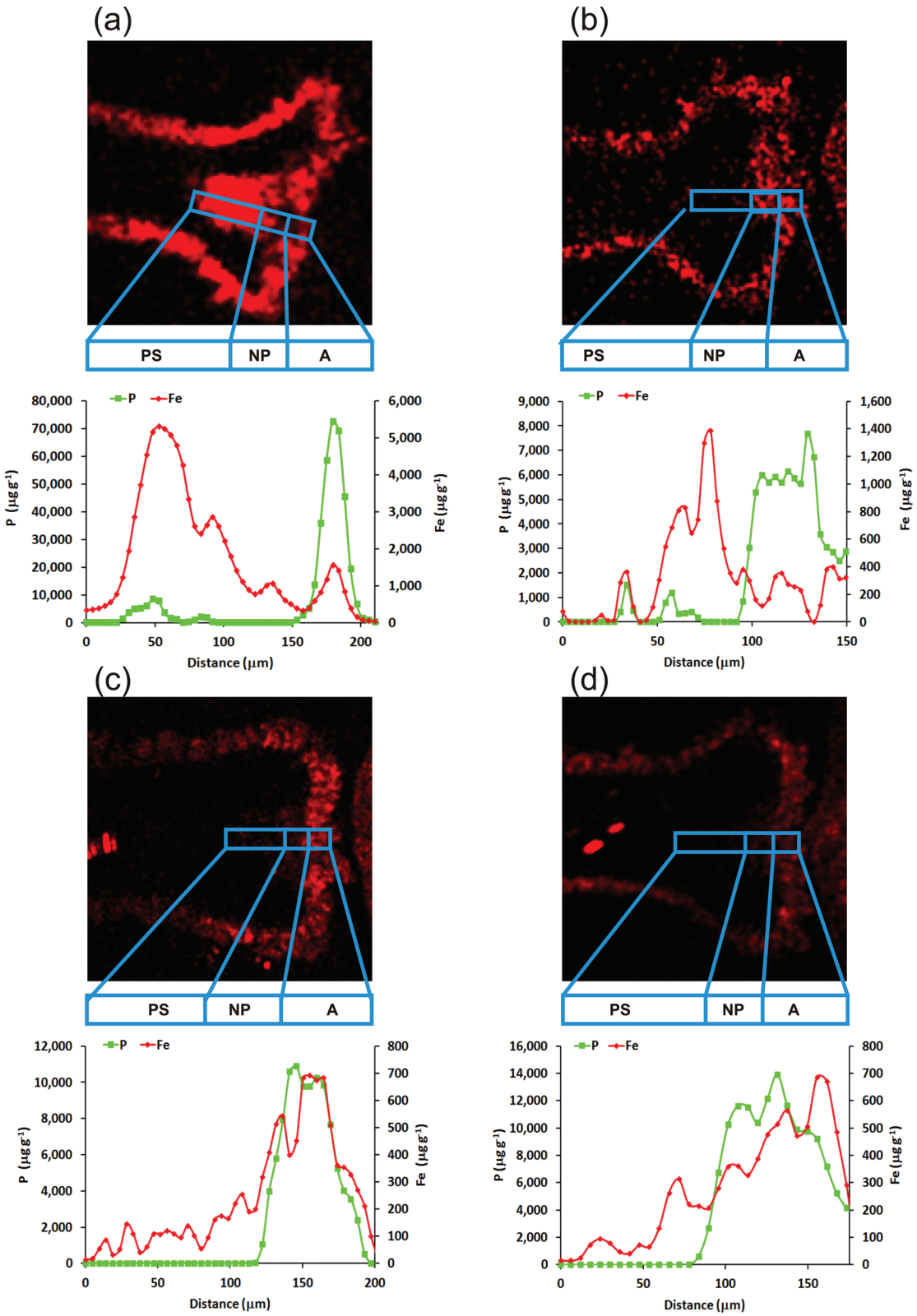

Fig. 3. Fe localization maps and Fe and P micro-PIXE profiling in crease tissues (vascular tissue, nucellar projection, aleurone transfer cells) of grains of *A. kotschyi* acc. 3790 (A), *T. aestivum* L. IITR26 (B), *T. aestivum* Cv. WH291 (C), and *T. aestivum* Cv. WL711 (D).

genotypes was the presence of a significantly less amount of iron in the endosperm. The iron-rich outermost layer of aleurone was the major tissue where iron accumulated in all cases, but iron was not mobilized into endosperm.

Speciation and coordination of environment of grain iron

In Fe K-edge XANES, the relative fraction of valence states of the metal can be deduced from the energy shift of the absorption edge (Arčon *et al.*, 2007; Küezma *et al.*, 2009; Ortega *et al.*, 2012). The iron oxidation state was first examined in ground and homogenized seed material pressed into pellets at XAS beamline of Elettra-Synchrotron (Trieste, Italy). The ferrous form could rarely be detected due to oxidation of iron during the grinding procedure (data not shown). To avoid oxidation, Fe-K edge XANES spectra were measured on intact seeds at C beamline (HASYLAB, Hamburg, Germany).

Normalized Fe XANES spectra were obtained for the intact grain samples and reference compounds with well-established Fe^{2+} and Fe^{3+} valence states and local symmetry of the Fe atom neighbourhood (Fig. 4). The Fe K-edge shifted to higher energies with increasing average Fe valence state. The iron compounds Fe(II) glutathione, Fe(II) sulphate, Fe(II) phytate, Fe(II) oxalate, Fe(III) phytate, Fe(III) sulphate, Fe(III) citrate, Fe(III) phosphate (Fig. 4), and Fe_3O_4, α-FeOOH, and Fe_2O_3 (not shown), with known Fe valence states, Fe^{2+} and Fe^{3+}, and known local symmetry of Fe atom neighbourhood, were selected for reference. A shift of about 4.5 eV was found between the spectra of the Fe^{2+} and Fe^{3+} compounds (Fig. 4), in agreement with previous observations (Arčon *et al.*, 2007). The symmetry of the Fe cation and the type of Fe ligand were reflected in a characteristic shape of the Fe K-edge and pre- and post-edge resonance structures in the XANES spectrum. The energy position of the Fe K-edge in the intact grain samples was close to the edge position of Fe^{3+} compounds (Fig. 4), confirming that iron in the sample was predominantly ferric ion.

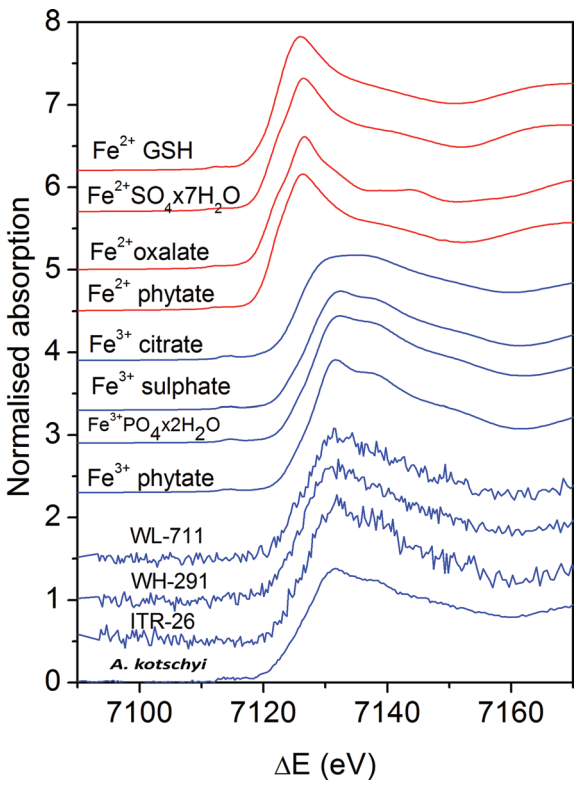

Fig. 4. Fe K-edge XANES spectra of grain samples from *A. kotschyi* acc. 3790, *T. aestivum* L. IITR26, *T. aestivum* Cv. WH291, and *T. aestivum* Cv. WL711 and reference Fe compounds with octahedral coordination and valence states Fe^{2+} and Fe^{3+}: Fe(II) glutathione (GSH), Fe(II) sulphate, Fe(II) oxalate, Fe(II) phytate, Fe(III) citrate, Fe(III) sulphate, Fe(III) phosphate, and Fe(III) phytate) (this figure is available in colour at *JXB* online).

The Fe XANES spectra of grains were fitted with linear combination of XANES spectra of the aforesaid reference compounds (Küezma *et al.*, 2009; Dominko *et al.*, 2010). The linear combination fitting analysis determined the relative amount of Fe(II) (14–23%) and Fe(III) (77–86%) cations in the samples with a precision of ± 3% (Fig. 5). In *A. kotschyi* acc. 3790, *T. aestivum* WH291, and *T. aestivum* WL711), the best fit was obtained with combination of Fe(II) phytate, Fe(III) phytate, and Fe(III) sulphate (Fig. 5A,C,D), while in *T. aestivum* IITR 26 the best fit was with Fe(II) phytate and Fe(III) phytate (Fig. 5B).

The results indicated the presence of Fe-O-P-R and Fe-O-S-R coordination in the local environment of ferrous and ferric iron, respectively. However, the estimates of iron complexes comprising Fe-O-P-R and Fe-O-S-R were made with rather low precision (± 10%). This was due to relatively small differences between Fe phytate and Fe sulphate spectra and relatively high noise of the grain spectra. Thus, this study determines the fractions of Fe(II) and Fe(III) oxidation states in grains of the four genotypes (Fig. 5). As far as is known, the proportion of iron species in wheat grains has not been reported earlier.

Co-occurrence analysis of iron with phosphorus and sulphur

Spatial distribution of P and S was studied in the grain cross-sections of all genotypes to examine their co-occurrence with iron using micro-PIXE. P was predominantly present in the aleurone, the scutellum, and to some extent, the embryo region, whereas it was very low in the endosperm (Fig. 6). On the other hand, in addition to the aleurone, S was visualized in the form of several scattered spots in the endosperm region. The S spots were proportionately fewer in the low-iron cultivars than in the land race and its wild relative (Fig. 6). The pattern of the amount of spots of S in endosperm coincided with that of iron in each genotype. In order to analyse in more detail the co-occurrence of iron, phosphorus, and sulphur in the tissues of the mineral transport route of wheat grains, a zoomed area of the crease was scanned by micro-PIXE.

In the low-iron cultivars, iron signals were detected in an increasing gradient from the pigment strand to the nucellar projection and then to the aleurone transfer cells.

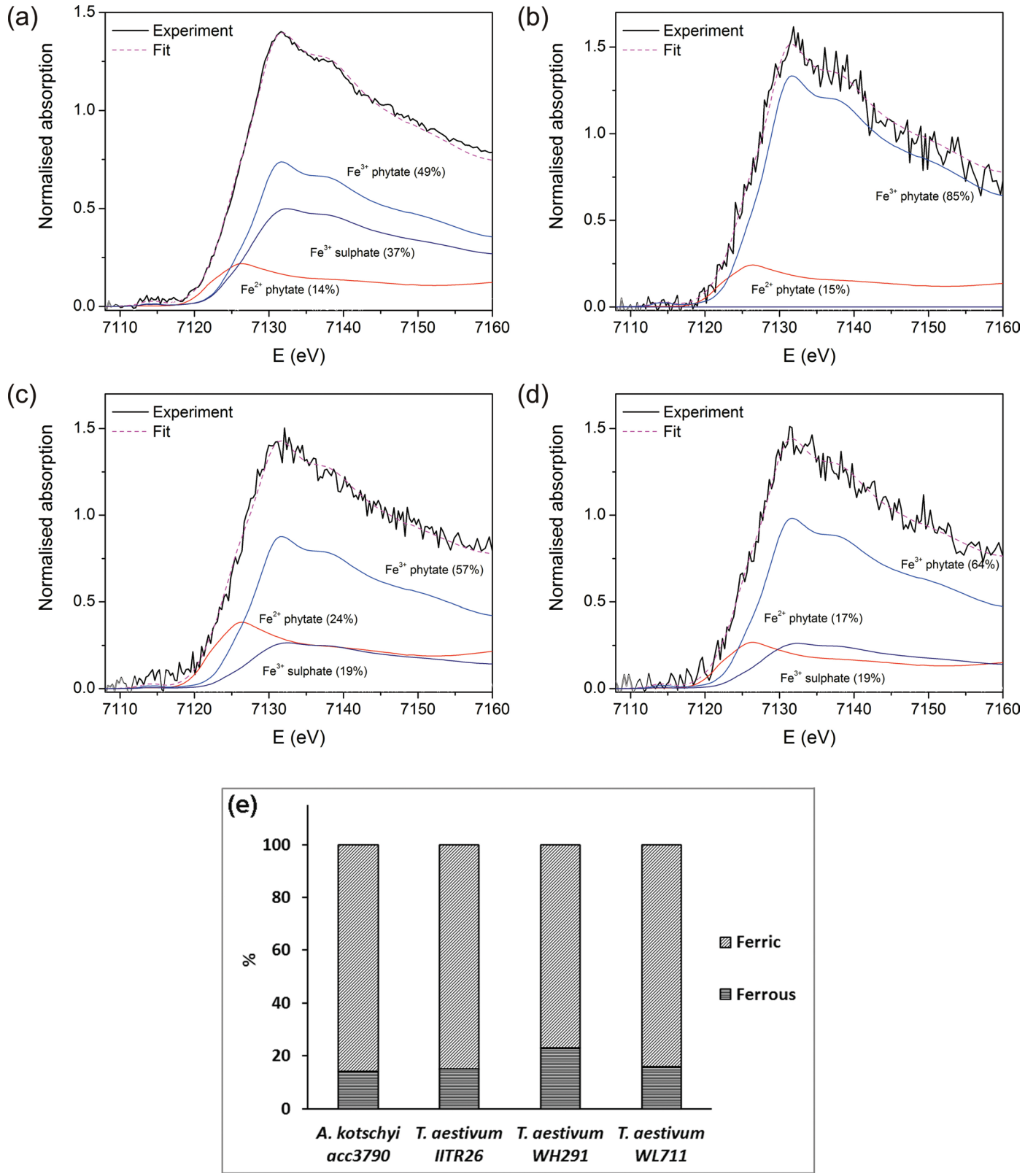

Fig. 5. (A–D) Fe XANES spectra measured on the intact grains of *A. kotschyi* acc. 3790 (A), *T. aestivum* L. IITR26 (B), *T. aestivum* Cv. WH291 (C), and *T. aestivum* Cv. WL711 (D). Solid black lines, experiment; dashed magenta line, best-fit linear combination of XANES profiles of Fe(II) phytate, Fe(III) phytate, and Fe(III) sulphate. (E) Proportion of ferric and ferrous iron in the grains (this figure is available in colour at *JXB* online).

A high-concentration peak of P overlapping with iron was evident in the aleurone transfer cells (Fig. 3C,D). The pigment strand and the nucellar projection had low iron and very little phosphorus. Sulphur was co-localized with iron in the nucellar projection cells (WH291, Mander's overlap coefficient, R = 0.824; WL711, R = 0.625), which gradually

reduced in the aleurone transfer cells (Supplementary Fig. S3C,D). In comparison to the nucellar projection, the concentration of S was significantly lesser in the pigment strand and the aleurone transfer cells.

In the case of the high-iron land race and its wild relative, Fe accumulation was more prominent in the pigment stand and the nucellar projection, respectively, in comparison to the aleurone transfer cells. P concentration was significantly high in the aleurone transfer cells. S accumulation was distinctly higher in the pigment strand as well as the nucellar projection (Supplementary Fig. S3A,B). The preferential occurrence of S in the crease tissues, the lesser concentration of Fe in the aleurone transfer cells, and the more spots of Fe in the endosperm in the wild relative and the land race suggest that S may have a role in iron transport and accumulation in the grains.

Discussion

To design strategies for the iron biofortification of cereals, it is important to understand the tissue-specific localization of the elements at high resolution and the chemical state of the deposited minerals. This work performed iron imaging studies on four genotypes that show differences in grain iron concentration (Supplementary Fig. S1A). A comparison of thousand kernel weight shows that the total iron uptake in the four genotypes is fairly comparable (Supplementary Fig. S1C). Although the concentration effect has been pointed out to be due to small seed size (Calderini and Ortiz-Monasterio, 2003; Oury *et al.*, 2006), the small-seeded *Triticum* and wild *Aegilops* species have proved useful genetic materials for micronutrient enhancement in wheat cultivars (Rawat *et al.*, 2009*a*,*b*; Tiwari *et al.*, 2010). This information can be helpful to understand how minerals are transported and deposited in grains of different genotypes.

XRF imaging of the crease region of grains showed distinct differences in the pattern of iron distribution in the four genotypes (Fig. 1). Micro-PIXE imaging further corroborated the XRF results, affirming that iron allocation tends to be higher in the pigment strand and the nucellar projection of the high-iron genotypes. The surplus iron transported to the grains of high-iron genotypes appears to get stuck in the vascular and nucellar projection tissues. In the case of the low-iron cultivars, the crease aleurone cells contained more iron than the vascular and nucellar projection cells (Fig. 2C–F). The X-ray fluorescence imaging (XRF and PIXE) suggested that iron accumulation shifted from the vascular bundle to the nucellar projection and the aleurone as the land races were improved by breeders to develop high-yielding cultivars (Fig. 3). The results are in agreement with the previous reports which found a prevalence of iron in vascular cells and a gradual decrease in its concentration from the vascular bundle and the nucellar projection to the endosperm, suggesting a critical role of the vascular bundle and the nucellar projection in regulating mineral transport towards the endosperm (Cvitanich *et al.*, 2010; Stomph *et al.*, 2011).

In wheat grains, most of the iron is believed to be largely complexed with phytic acid via ionic associations with negatively charged phosphates in aleurone globoids (Regvar *et al.*, 2011). However, very little is known about the proportion of chemical forms of iron (ferric or ferrous) present within wheat grains. Recent developments in the area of synchrotron-based spectroscopy techniques have fostered Fe K-edge XANES as a reliable technique to obtain information about the oxidation state and molecular geometry of elements in biological samples *in situ* without the need for sample preparation that may cause alterations in chemical species (Ortega *et al.*, 2012). Fitting linear combinations of reference XANES spectra to unknown XANES spectra is a reliable approach to determine the average valence state of an element in a sample. The reference compounds should have known valence states of the element to be analysed, with similar symmetry, the same type of neighbour atoms in the nearest coordination shells, and a similar local structure (Arčon *et al.*, 2007; Küezma *et al.*, 2009). As different Fe compounds produce different Fe K-edge profiles, linear combination fitting analysis helps to identify not only the relative amount of Fe(II) and Fe(III) valence states, but also the abundant elements in local chemical environment of Fe in the sample. Implementation of 'bulk' Fe K-edge XANES on intact grains resolved iron speciation as being 77–86 ± 3% ferric and the remainder as ferrous in mature seeds. It was of interest to study other elements in coordination with Fe(II) and Fe(III). The results suggest the storage of ferrous iron, possibly as Fe(II) phytate. Recently, phytic acid has been reported to sequester both Fe(II) and Fe(III) (Quirrenbach *et al.*, 2009; Bretti *et al.*, 2012a,b). The present results showed that most of the Fe(III) was in association with O and P. About 19% of trivalent iron was found in coordination of O and S. The results agree with the fact that P and S are major constituents of iron-binding compounds in grains. Phytic acid is known to be the predominant form of Fe, O, and P compounds in grains. It can be speculated that Fe may be associated with biological sulphate (Steinfurth *et al.*, 2012), metalloproteins (such as ferritin, comprising of mineral centre of ferric ions linked by oxygen atoms), or any other organic or bioinorganic complexes present in grains. The Fe, O, and S compounds may also be indicative of the presence of sulphate bridges between two ferric ions, coordinated to two phytate ions (Thompson and Erdman, 1982). The spectra for Fe, O, and S complexes were absent in the grains of IITR 26. It is possible that the iron compounds, having local environment of O and S, may be present in *T. aestivum* L. IITR26 in an amount lesser than the sensitivity limit of bulk XANES.

Co-localization of the lighter elements P and S was analysed along with iron to understand their co-occurrence with iron in the grains. The iron distribution followed closely the pattern observed for P in aleurone and scutellum (Fig. 6). It is likely that iron is bound to *myo*-inositol 1,2,3,4,5,6-hexakisphosphate, forming insoluble complexes in the phytin globoids of the aleurone, the scutellum, and the embryo (Perronnet *et al.*, 2000). The very low levels of P in the endosperm suggest that Fe may be associated in complexes other than phytic acid in the endosperm. In a recent study of high-resolution secondary ion mass spectrometry (NanoSIMS) images, low P signals were reported in starch grains of the endosperm, presumably in the

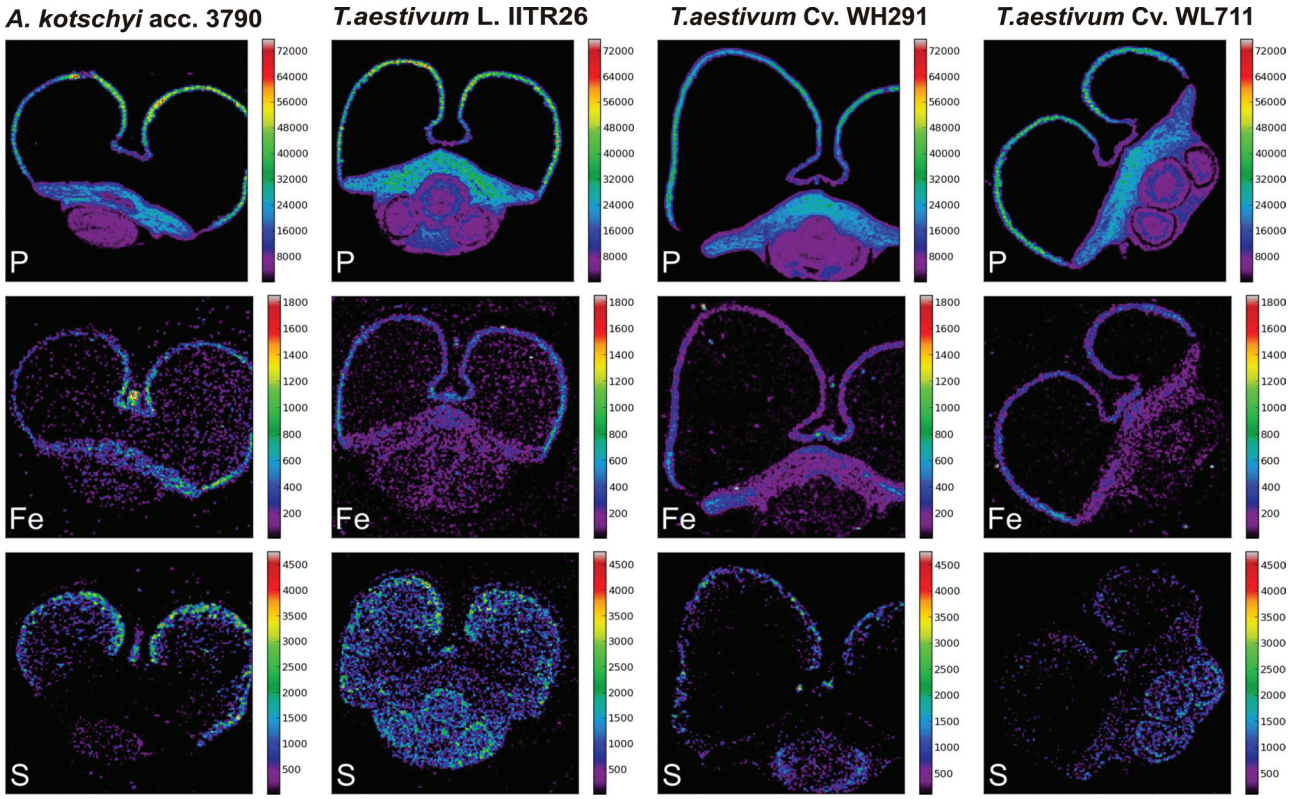

Fig. 6. Quantitative micro-PIXE images showing localization of P, S, and Fe in cross-sections of seeds of *A. kotschyi* acc. 3790, *T. aestivum* L. IITR26, *T. aestivum* Cv. WH291, and *T. aestivum* Cv. WL711. Colour bars indicate element concentrations in μg (g dryweight)$^{-1}$.

form of lysophospholipids. On the other hand, Fe surrounding the starch grains and in the nuclei of endosperm cells might be associated with ferritin or other proteins (Moore *et al.*, 2010).

The present study noticed that the proportion of Fe spots coincided with those for S in the endosperm. The proportional association in the contrasting genotypes suggested a probable role of sulphur complexes or sulphur proteins in iron mobilization in the endosperm (Fig. 6). It was, therefore, relevant to analyse the allocation of Fe, P, and S in the crease tissues. Distinct patterns of occurrence of Fe, P, and S were observed in the vascular strand, the nucellar projection, and the aleurone transfer cells.

In the low-iron cultivars, the co-accumulation of Fe and S was noticed in the nucellar projection, whereas the aleurone transfer cells were richer in Fe and P. It may be possible that Fe is bound to sulphur-rich peptides in the nucellar projection and that these sulphur complexes play critical role in iron transport at the maternal–filial interface. High levels of expression of several metal homeostasis genes have been reported in the nucellar projection transfer cells of developing barley grains (Tauris *et al.*, 2009). This is in agreement with the prevalence of S in the nucellar projection of wheat.

The distribution of Fe, P, and S in the high-iron land race and its wild relative was in contrast to that in the low-iron cultivars. Iron and phosphorous were predominant in different tissues in the high-iron genotypes, but co-localized in aleurone transfer cells in the low-iron cultivars (Fig. 3). A significant amount of iron in the vascular bundle and the nucellar projection of the high-iron genotypes is free from phosphorus and hence possibly more bioavailable. This agrees with the enhanced bioavailability of grain iron in *A. kotschyi* acc. 3790 and its wheat derivatives in comparison to *T. aestivum* L. WL711 (Salunke *et al.*, 2011). S was consistently present in the vascular bundle and the nucellar projection as well as the transfer cells in the high-iron genotypes (Supplementary Fig. S3A,B), but was predominant in the nucellar projection in low-iron cultivars (Supplementary Fig. S3C,D). The presence of S in all tissue types of the crease, including aleurone transfer cells, in high-iron genotypes, might lead to less Fe in the aleurone transfer cells (Fig. 6A,B). This may be due to mobilization of Fe towards the endosperm (Fig. 2A,B). However, Fe tends to localize more in the outermost layer of the endosperm (the aleurone) in all genotypes (Fig. 2E). The transcriptome and proteome of the nucellar projection (the chalazal as well as the transfer cells) of contrasting wheat genotypes need to be examined at the grain-filling stage to understand the possible role of S-containing compounds in iron loading in the endosperm. However, biofortification approaches may succeed by enhancing the efflux of iron to endosperm from nucellar projection and aleurone transfer cells.

In conclusion, this study illustrates the localization of iron in wheat genotypes with contrast in grain iron content. Striking differences were noticed in the Fe, P, and S distribution patterns along the route from the maternal to the filial tissues in the wild relative, the land race, and the low-iron cultivars. The results suggest that the development of

high-yielding wheat cultivars has led to the selection of varieties in which iron transport and localization shifted from the maternal tissue to the filial tissue aleurone. Although it is not known whether there is a negative association between iron in the endosperm and the yield/quality of wheat grain, little iron is transported to endosperm tissue. This report is the first estimate of the proportion of Fe species in mature grains: 14–23 ± 3% is ferrous and the rest is ferric. It remains to be examined if the relative proportions of ferrous and ferric species and the spatial differences in the localization of iron and phosphorous in grains of different wheat genotypes influence the bioavailability of grain iron in a wheat diet.

Supplementary material

Supplementary data are available at *JXB* online.

Supplementary Fig. S1. Iron concentration in mature grains of the four genotypes, transverse sections of the crease regions and the route of mineral transport, and thousand kernel weights of the four genotypes.

Supplementary Fig. S2. Marked tissues for the calculation of iron concentration in cross-sections of whole grains and crease tissues of the four genotypes.

Supplementary Fig. S3. Iron, phosphorous, and sulphur co-localization map and micro-PIXE profiles in the crease tissues of the four genotypes.

Acknowledgements

This work was supported by the Department of Biotechnology (DBT, Government of India), the Slovenian Research Agency research programme (P1-0112, P-0212) and DESY and the European Community's Seventh Framework Programme (FP7/2007–2013) under grant agreement CALIPSO n_ 312284 (EU Support of Access to Synchrotrons/FELs in Europe). Micro-PIXE methodology and instrumentation at JSI was upgraded within the project 7FP EU No. 227012 'SPIRIT'. Access to synchrotron radiation facilities of CLS (project 14–3657), HASYLAB (project I-20110511 EC) and Elettra (projects 20110086 and 20115112) is acknowledged. IAEA framework of coordinated research project 16796 "Applications of synchrotron radiation for environmental sciences and materials research for development of environmentally friendly resources" (CSI, KV) is acknowledged. Renfei Feng of CLS, Giuliana Aquilanti and Luca Olivi of Elettra, and Roman Chernikov and Edmund Welter of HASYLAB are acknowledged for expert advice on beamline operation. Harcharan S. Dhaliwal of Eternal University is acknowledged for providing the grains. S.P.S. acknowledges DBT for supporting visit to CLS, Canada. R.T. acknowledges J. C. Bose fellowship, Department of Science and Technology, Government of India.

References

Arčon I, Kolar J, Kodre A, Hanžel D, Strlič M. 2007. XANES analysis of Fe valence in iron gall inks. *X-Ray Spectrometry* **36,** 199–205.

Bretti C, Cigala RM, De Stefano C, Lando G, Sammartano S. 2012a. Interaction of phytate with Ag^+, CH_3Hg^+, Mn_2^+, Fe_2^+, Co_2^+, and VO_2^+: stability constants and sequestering ability. *Journal of Chemical and Engineering Data* **57,** 2838–2847.

Bretti C, Cigala RM, Lando G, Milea D, Sammartano S. 2012b. Sequestering ability of phytate toward biologically and environmentally relevant trivalent metal cations. *Journal of Agricultural and Food Chemistry* **60,** 8075–8082.

Calderini DF, Ortiz-Monasterio I. 2003. Grain position affects grain macronutrient and micronutrient concentrations in wheat. *Crop Science* **43,** 141–151.

Conte SS, Walker EL. 2011. Transporters contributing to iron trafficking in plants. *Molecular Plant* **4,** 464–476.

Curie C, Panaviene Z, Loulergue C, Dellaporta SL, Briat JF, Walker EL. 2001. Maize yellow stripe1 encodes a membrane protein directly involved in Fe(III) uptake. *Nature* **409,** 346–349.

Cvitanich C, Przybyłowicz WJ, Urbanski DF, Jurkiewicz AM, Mesjasz-Przybyłowicz J, Blair MW, Astudillo C, Jensen EØ, Stougaard J. 2010. Iron and ferritin accumulate in separate cellular locations in *Phaseolus* seeds. *BMC Plant Biology* **10,** 26.

Dominko R, Sirisopanaporn C, Masquelier C, Hanzel D, Arčon I, Gaberscek M. 2010. On the origin of the electrochemical capacity of $Li_2Fe_{0.8}Mn_{0.2}SiO_4$. *Journal of the Electrochemical Society* **157,** A1309-A1316.

Grimm KA, Sullivan KM, Alasfoor D, Parvanta I, Suleiman AJM, Kaur M, Al-Hatmi FO, Ruth LJ. 2012. Iron-fortified wheat flour and iron deficiency among women. *Food and Nutrition Bulletin* **33,** 180–185.

Hansen TH, Lombi E, Fitzgerald M, *et al.* 2012. Losses of essential mineral nutrients by polishing of rice differ among genotypes due to contrasting grain hardness and mineral distribution. *Journal of Cereal Science* **56,** 307–315.

Hell R, Stephan UW. 2003. Iron uptake, trafficking and homeostasis in plants. *Planta* **216,** 541–551.

Küezma M, Dominko R, Hanzel D, Kodre A, Arcon I, Meden A, Gaberscek M. 2009. Detailed in situ investigation of the electrochemical processes in Li_2FeTiO_4 cathodes. *Journal of the Electrochemical Society* **156,** A809–A816.

Lee S, Kim Y-S, Jeon US, Kim Y-K, Schjoerring JK, An G. 2012. Activation of rice nicotianamine synthase 2 (OsNAS2) enhances iron availability for biofortification. *Molecules and Cells* **33,** 269–275.

Lyubenova L, Pongrac P, Vogel-Mikuš K, *et al.* 2012. Localization and quantification of Pb and nutrients in *Typha latifolia* by micro-PIXE. *Metallomics* **4,** 333–341.

Lombi E, Smith E, Hansen TH, Paterson D, De Jonge MD, Howard DL, Persson DP, Husted S, Ryan C, Schjoerring JK. 2011. Megapixel imaging of (micro)nutrients in mature barley grains. *Journal of Experimental Botany* **62,** 273–282.

Ma JF, Nomoto K. 1996. Effective regulation of iron acquisition in graminaceous plants. The role of mugineic acids as phytosiderophores. *Physiologia Plantarum* **97,** 609–617.

Mesjasz-Przybyłowicz J, Przybyłowicz WJ. 2002. Micro-PIXE in plant sciences: present status and perspectives. *Nuclear Instruments and Methods in Physics Research B* **189,** 470–481.

Moore KL, Schröder M, Lombi E, Zhao F-J, McGrath SP, Hawkesford MJ, Shewry PR, Grovenor CRM. 2010. NanoSIMS analysis of arsenic and selenium in cereal grain. *New Phytologist* **185,** 434–445.

Morrissey J, Guerinot ML. 2009. Iron uptake and transport in plants: the good, the bad, and the ionome. *Chemical Reviews* **109,** 4553–4567.

Ortega R, Carmona A, Llorens I, Solari PL. 2012. X-ray absorption spectroscopy of biological samples. A tutorial. *Journal of Analytical Atomic Spectrometry* **27,** 2054–2065.

Oury F, Leenhardt F, Remesy C, Chanliaud E, Duperrier B, Balfourier F, Charmet G. 2006. Genetic variability and stability of grain magnesium, zinc and iron concentrations in bread wheat. *European Journal of Agronomy* **25,** 177–185.

Patrick JW, Offler CE. 2001. Compartmentation of transport and transfer events in developing seeds. *Journal of Experimental Botany* **52,** 551–64.

Pearson JN, Rengel Z, Jenner CF, Graham RD. 1995. Transport of zinc and manganese to developing wheat grains. *Physiologia Plantarum* **95,** 449–455.

Perronnet K, Schwartz C, Emilie G, Morel JL. 2000. Availability of cadmium and zinc accumulated in the leaves of *Thlaspi caerulescens* incorporated into soil. *Plant and Soil* **227,** 257–263.

Pongrac P, Vogel-Mikuš K, Regvar M, Vavpetič P, Pelicon P, Kreft I. 2011. Improved lateral discrimination in screening the elemental composition of buckwheat grain by micro-PIXE. *Journal of Agricultural and Food Chemistry* **59,** 1275–1280.

Quirrenbach HR, Kanumfre F, Rosso ND, Carvalho Filho MA. 2009. Comportamento do ácido fítico na presença de Fe(II) e Fe(III). *Ciência e Tecnologia de Alimentos* **29,** 24–32.

Ravel B, Newville M. 2005. ATHENA, ARTEMIS, HEPHAESTUS: data analysis for X-ray absorption spectroscopy using IFEFFIT. *Journal of Synchrotron Radiation* **12,** 537–541.

Rawat N, Tiwari VK, Neelam K, Randhawa GS, Chhuneja P, Singh K, Dhaliwal HS. 2009a. Development and characterization of *Triticum aestivum–Aegilops kotschyi* amphiploids with high grain iron and zinc contents. *Plant Genetic Resources* **7,** 271–280.

Rawat N, Tiwari VK, Singh N, Randhawa GS, Singh K, Chhuneja P, Dhaliwal HS. 2009b. Evaluation and utilization of *Aegilops* and wild *Triticum* species for enhancing iron and zinc content in wheat. *Genetic Resources and Crop Evolution* **56,** 53–64.

Regvar M, Eichert D, Kaulich B, Gianoncelli A, Pongrac P, Vogel-Mikuš K, Kreft I. 2011. New insights into globoids of protein storage vacuoles in wheat aleurone using synchrotron soft X-ray microscopy. *Journal of Experimental Botany* **62,** 3929–3939.

Ryan CG. 2000. Quantitative trace element imaging using PIXE and the nuclear microprobe. *International Journal of Imaging Systems and Technology* **11,** 219–230.

Salunke R, Neelam K, Rawat N, Tiwari VK, Randhawa GS, Dhaliwal HS, Roy P. 2011. Bioavailability of iron from wheat *Aegilops* derivatives selected for high grain iron and protein contents. *Journal of Agricultural and Food Chemistry* **59,** 7465–7473.

Solé VA, Papillon E, Cotte M, Walter P, Susini J. 2007. A multiplatform code for the analysis of energy-dispersive X-ray fluorescence spectra. *Spectrochimica Acta B* **62,** 63–68.

Steinfurth D, Zörb C, Braukmann F, Mühling KH. 2012. Time-dependent distribution of sulphur, sulphate and glutathione in wheat tissues and grain as affected by three sulphur fertilization levels and late S fertilization. *Journal of Plant Physiology* **169,** 72–77.

Stomph TJ, Choi EY, Stangoulis JCR. 2011. Temporal dynamics in wheat grain zinc distribution: is sink limitation the key? *Annals of Botany* **107,** 927–937.

Tanaka K, Fujimaki S, Fujiwara T, Yoneyama T, Hayashi H. 2007. Quantitative estimation of the contribution of the phloem in cadmium transport to grains in rice plants (*Oryza sativa* L.). *Soil Science and Plant Nutrition* **53,** 72–77.

Tauris B, Borg S, Gregersen PL, Holm PB. 2009. A roadmap for zinc trafficking in the developing barley grain based on laser capture microdissection and gene expression profiling. *Journal of Experimental Botany* **60,** 1333–1347.

Thompson DB, Erdman JW. 1982. Structural model for ferric phytate: implications for phytic acid analysis. *Cereal Chemistry* **59,** 525–528.

Tiwari VK, Rawat N, Neelam K, Kumar S, Randhawa GS, Dhaliwal HS. 2010. Substitutions of 2S and 7U chromosomes of *Aegilops kotschyi* in wheat enhance grain iron and zinc concentration. *Theoretical and Applied Genetics* **121,** 259–269.

Tolrà R, Vogel-Mikuš K, Hajiboland R *et al.* 2011. Localization of aluminium in tea (*Camellia sinensis*) leaves using low energy X-ray fluorescence spectro-microscopy. *Journal of Plant Research* **124,** 165–172.

Vogel-Mikuš K, Pelicon P, Vavpetič P, Kreft I, Regvar M. 2009. Elemental analysis of edible grains by micro-PIXE: common buckwheat case study. *Nuclear Instruments and Methods in Physics Research B* **267,** 2884–2889.

Vogel-Mikuš K, Simcic J, Pelicon P, Budnar M, Kump P, Necemer M, Mesjasz-Przybyłowicz J, Przybyłowicz WJ, Regvar M. 2008. Comparison of essential and non-essential element distribution in leaves of the Cd/Zn hyperaccumulator *Thlaspi praecox* as revealed by micro-PIXE. *Plant, Cell and Environment* **31,** 1484–1496.

Zhang Y, Shi R, Rezaul KM, Zhang F, Zou C. 2010. Iron and zinc concentrations in grain and flour of winter wheat as affected by foliar application. *Journal of Agricultural and Food Chemistry* **58,** 12268–12274.

Zhao FJ, Su YH, Dunham SJ, Rakszegi M, Bedo Z, McGrath SP, Shewry PR. 2009. Variation in mineral micronutrient concentrations in grain of wheat lines of diverse origin. *Journal of Cereal Science* **49,** 290–295.

Pattern of iron distribution in maternal and filial tissues in wheat grains with contrasting levels of iron

Sudhir P. Singh, Katarina Vogel-Mikuš, Iztok Arčon, Primož Vavpetič, Luka Jeromel, Primož Pelicon, Jitendra Kumar, Rakesh Tuli

Figure Legend

Figure S1. (a) Iron concentration in mature grains of the four genotypes, estimated by Inductively coupled plasma mass spectrometry (ICP-MS; 7700x Agilent Technologies, Santa Clara, CA). The error bars indicate standard deviation in three independent biological replicates. (b) Transverse section of crease region of wheat grain (RM2265, CTR6000 Leica Microsystems, Germany; TES99 Medite, Germany), and the route of mineral transport. (c) Thousand kernel weights (TKW) of the four genotypes. TKW was measured as described in Su *et al.*, 2011.

Figure S2. Marked tissues for the calculation of iron concentration in cross section of whole grain (left) and crease tissues (right) of (a) *A. kotschyi* acc. 3790, (b) *T. aestivum* L. IITR26, (c) *T. aestivum* Cv. WH291 and (d) *T. aestivum* Cv. WL711.

Figure S3. Iron (red), phosphorous (green) and sulphur (blue) co-localization map and µ-PIXE profile in crease tissues (vascular tissue, nucellar projection, aleurone transfer cells) of grains of (a) *A. kotschyi* acc. 3790, (b) *T. aestivum* L. IITR26, (c) *T. aestivum* Cv. WH291 and (d) *T. aestivum* Cv. WL711.

Reference:

Su Z, Hao C, Wang L, Dong Y, Zhang X. 2011. Identification and development of a functional marker of TaGW2 associated with grain weight in bread wheat (*Triticum aestivum* L.). Theoretical and applied genetics. **122**, 211–23.

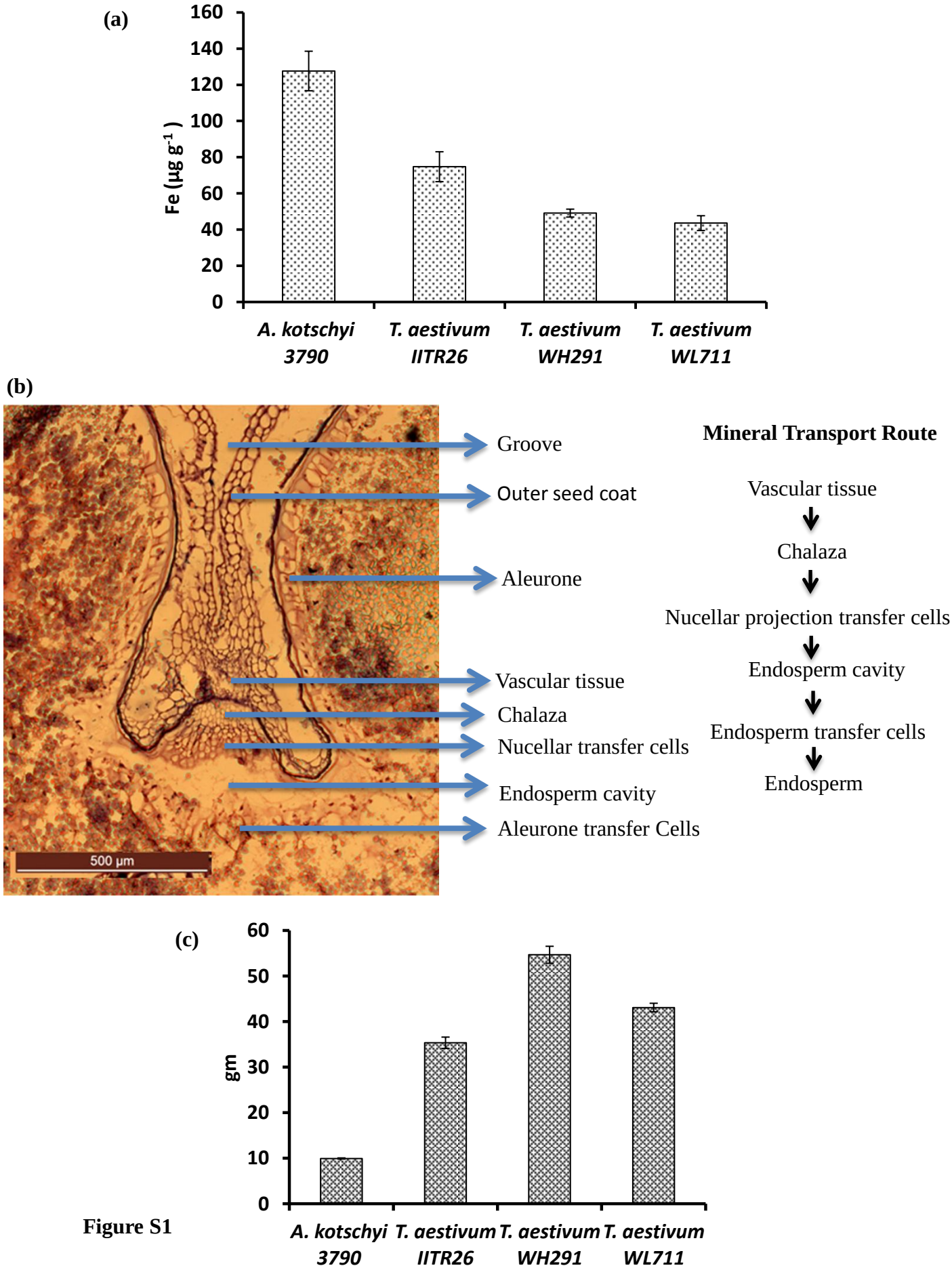
(a)
160
140
120
100
80
60
40
20
0
Fe (µg g-1)
A. kotschyi 3790
T. aestivum IITR26
T. aestivum WH291
T. aestivum WL711
(b)
Groove
Outer seed coat
Aleurone
Vascular tissue
Chalaza
Nucellar transfer cells
Endosperm cavity
Aleurone transfer Cells
500 µm
Mineral Transport Route
Vascular tissue
Chalaza
Nucellar projection transfer cells
Endosperm cavity
Endosperm transfer cells
Endosperm
(c)
60
50
40
30
20
10
0
gm
A. kotschyi 3790
T. aestivum IITR26
T. aestivum WH291
T. aestivum WL711

Figure S1

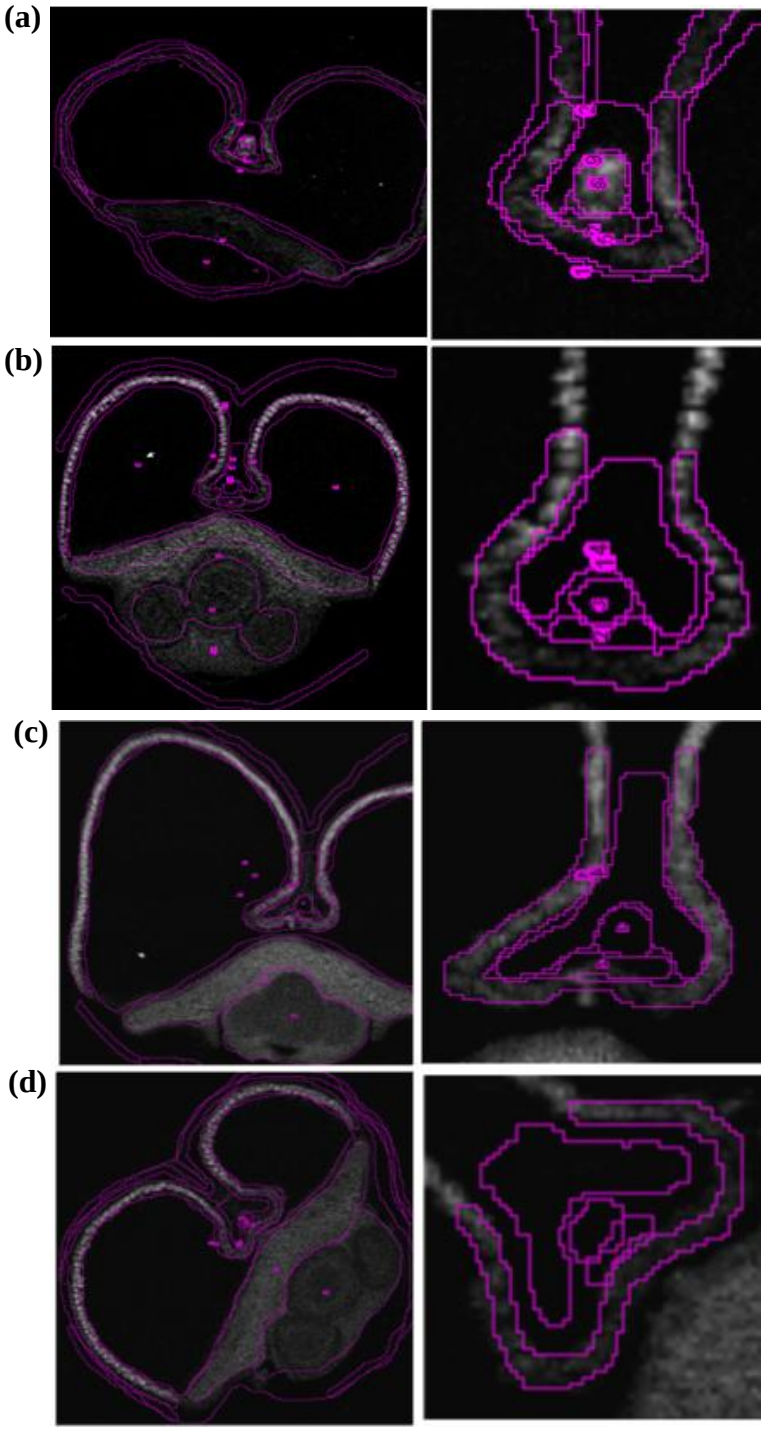

Figure S2

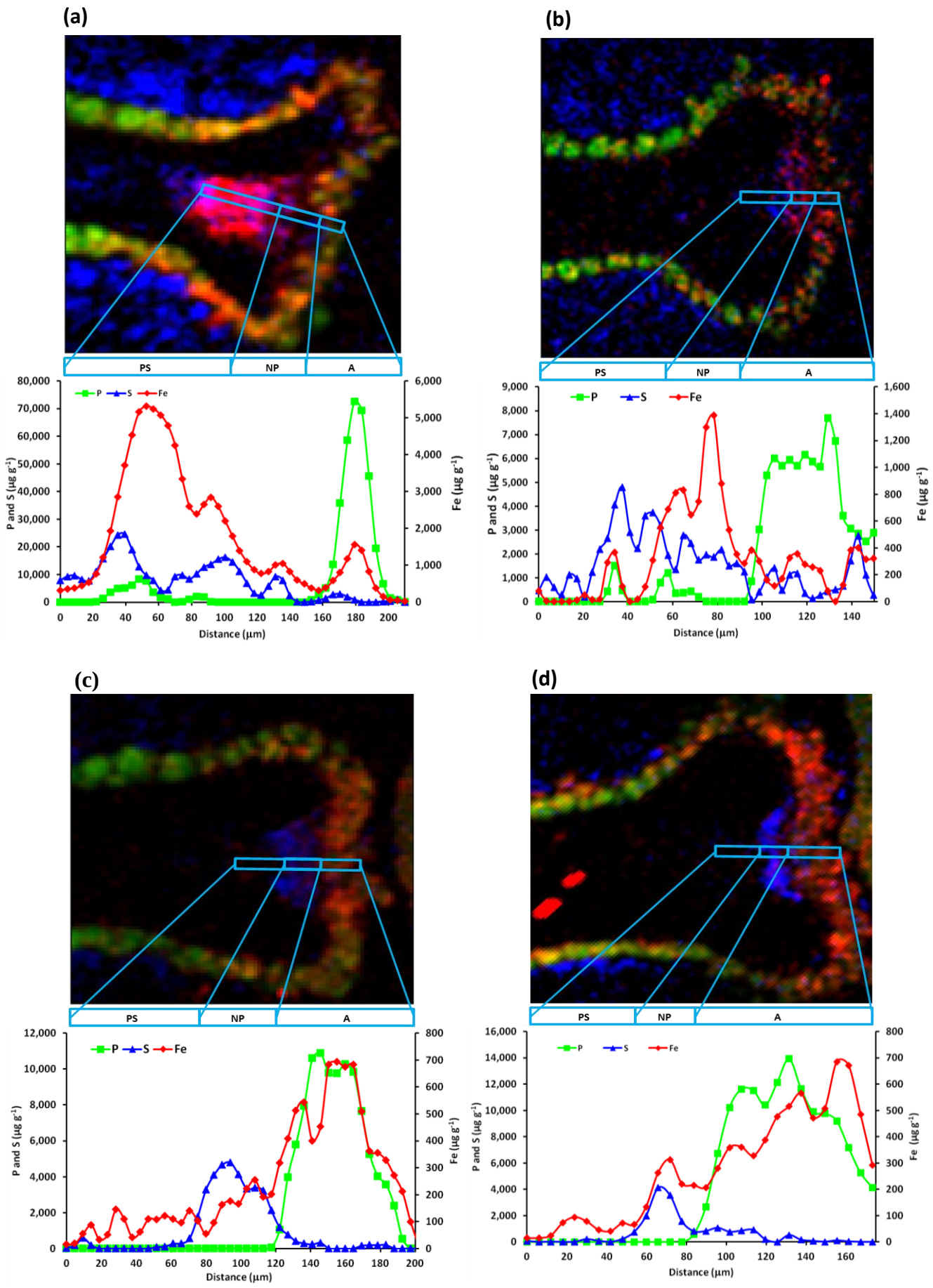
(a)
PS
NP
A
P
S
Fe
P and S (µg g-1)
Fe (µg g-1)
Distance (µm)
(b)
PS
NP
A
P
S
Fe
P and S (µg g-1)
Fe (µg g-1)
Distance (µm)
(c)
PS
NP
A
P
S
Fe
P and S (µg g-1)
Fe (µg g-1)
Distance (µm)
(d)
PS
NP
A
P
S
Fe
P and S (µg g-1)
Fe (µg g-1)
Distance (µm)

Figure S3